



Regional scaling of sea surface temperature with global warming levels in the CMIP6 ensemble

Josipa Milovac¹ · Maialen Iturbide¹ · Jesús Fernández¹ · José Manuel Gutiérrez¹ · Javier Diez-Sierra¹ · Richard G. Jones²

Received: 17 October 2023 / Accepted: 19 March 2024
© The Author(s) 2024

Abstract

Sea surface temperature (SST) and sea surface air temperature (SSAT) are commonly used as proxies for investigating the impact of climate change on oceans. These variables have been warming since pre-industrial times and are expected to continue to warm in the future under all Shared Socioeconomic Pathways (SSPs). However, they are warming in a spatially heterogeneous way, even with some cooling spots. In this work, we provide a general overview on the regional scaling of SST and SSAT with global warming, based on a 26-member CMIP6 ensemble. We utilize the global warming level (GWL) as a climate change dimension to analyze scaling patterns between sea temperature anomalies and the corresponding GWLs during the 21st century. This analysis is conducted globally, regionally, and on grid-point basis. The results show that SST and SSAT scale linearly with GWL at global scale, with scaling factors $\beta = 0.71 \pm 0.001$ K/K and $\beta = 0.86 \pm 0.001$ K/K, respectively. These results are robust, showing only minor differences between seasons, SSPs, and horizontal model resolutions. However, large differences emerge at regional scale, and the scaling of the two temperatures are strongly influenced by sea-ice. The lowest values are obtained for the Southern Ocean region, $\beta = 0.54 \pm 0.005$ K/K, projecting that the mean SST will increase only half as fast as the global mean temperature. These results provide valuable insight for refining the ocean IPCC reference regions, considering spatial homogeneity in terms of the regional response to global warming. A refinement of six ocean reference regions has been proposed.

Keywords Sea surface temperature · Ocean warming · Climate change · CMIP6 · IPCC · Reference regions · Regional warming sensitivity

1 Introduction

Sea surface temperature (SST) is a key ocean variable to investigate the impacts of climate change on both atmospheric and ocean processes. It represents an interface through which the interaction between the ocean surface and the atmosphere occurs and, as such, its variability affects the weather and climate on all temporal and spatial scales (Alves et al. 2018; Bulgin et al. 2020; Levine et al. 2021; Middlemas et al. 2019; Ruela et al. 2020). For example, sea-

sonal and interannual SST variability modulates upwelling and downwelling, the physical processes that have major influence on marine ecosystems (Kessler et al. 2022; Varela et al. 2018, 2022). While natural climate fluctuations, such as the El Niño Southern Oscillation (ENSO) phenomenon, play a significant role in the SST variability, leading to substantial increases during specific years and seasons (Bulgin et al. 2020; Cai et al. 2022), global SST changes as compared to pre-industrial (PI) times is primarily driven by climate change (Froelicher et al. 2018; Palmer et al. 2021).

The observed warming of the climate system is typically quantified by the anomalies of the global mean surface temperature (GMST), which merges global land surface air temperature (LSAT) and SST (Masson-Delmotte et al. 2021). On the other hand, estimates of global warming derived from Global Climate Model (GCM) simulations (e.g. from the Coupled Model Intercomparison Project, CMIP), typically use sea surface air temperature (SSAT, i.e. near-surface air

✉ Josipa Milovac
milovacj@unican.es

José Manuel Gutiérrez
gutierjm@ifca.unican.es

¹ Instituto de Física de Cantabria (IFCA), CSIC-Universidad de Cantabria, Santander, Spain

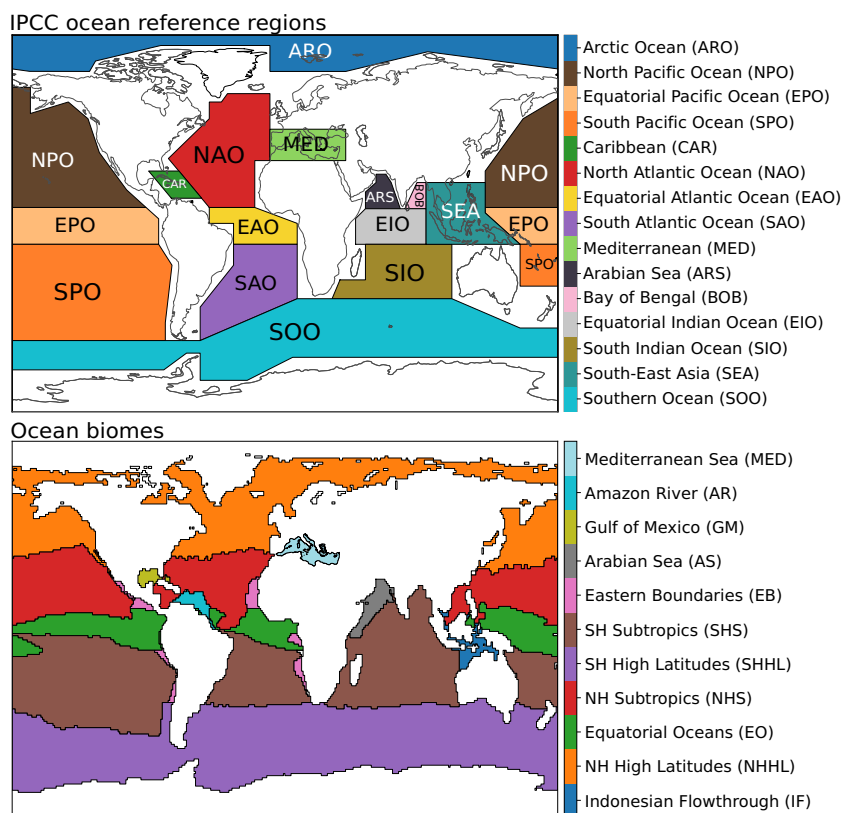
² Met Office Hadley Centre, Exeter, UK

temperature over oceans) instead of SST, and compute global surface air temperature (GSAT) using LSAT and SSAT. Even though the difference on the global scale between GMST and GSAT tends to be up to 10%, the term “global mean surface temperature” refers to both temperatures in most climate change studies (see Section 1.4.1 and Cross-Chapter Box 2.3 in IPCC, 2021). According to the latest IPCC report (Masson-Delmotte et al. 2021), GMST for the period 2011–2020 has increased by 1.09 °C since PI times (1850–1900), and it is projected to continue to rise by 1.0 to 5.7 °C by the end of the 21st century, depending on the Shared Socioeconomic Pathway (SSP). On the other hand, global mean SST has increased by 0.88°C since PI times and almost 70% of that increase (0.6 °C) happened in the last 40 years. This warming is not uniform over the globe. Parts of the Indian Ocean, western Equatorial Pacific Ocean (EPO, see Fig. 1), and western boundary currents respond faster to global warming, while the sea surface in the regions of eastern EPO, subpolar North Atlantic Ocean (NAO) and Southern Ocean (SOO) tend to warm at slower rates than the global average. A cooling has been observed in the NAO subregion known as the warming hole (Armour et al. 2016; Haumann et al. 2020; Keil et al. 2020), and in some parts of SOO (Auger et al. 2021; Xu et al. 2022). Various studies based on observations and GCM simulations project that the regional pattern of the future SST change will follow the historical trends, with intensity dependent on the SSP and the region, and some of the nega-

tive trends in SOO will change to positive (Masson-Delmotte et al. 2021).

Many of the studies on SST concentrate on past and current climate over limited areas. For example, multiple studies are centered on the SOO region, which show significantly slower ocean warming than the rest of the world (Adusumilli et al. 2020; Anderson and Mackintosh 2012; Armitage et al. 2018; Armour et al. 2016; Haumann et al. 2020), with sea-ice melting at a much slower pace than in other sea-ice regions (Rackow et al. 2022). On the other hand, the Arctic warms much faster, with a rate up to 4 times higher than the global average (Rantanen et al. 2022). This increase also affects SST in this region, especially in the warm seasons when sea-ice is melting and the SST increase is not limited by the sea-ice layer (Carton et al. 2015). Climate change effects on SST were explored by Froelicher et al. (2018), who focused on marine heatwaves (MHW) using CMIP5 simulations. Their results suggest that MHWs will become more frequent and intense due to global warming, with the Arctic and western EPO being affected the most. Ruela et al. (2020) investigated regional variability over eight non-sea-ice regions using CMIP5 simulations forced by two Representative Concentration Pathways (RCPs). They showed a higher SST response to climate change in the Northern Hemisphere (NH) than in the Southern Hemisphere (SH), especially in the Subtropical region. Garcia-Soto et al. (2021) provide an overview on the global SST projections as one of the few

Fig. 1 Set of regions for regional aggregation of SSAT and SST used to analyze regional response to global warming: (top) IPCC reference regions and (bottom) ocean biomes (Gutiérrez et al. 2021)



ocean climate change indicators based on the recent CMIP6 simulations.

As an alternative to the use of fixed future periods across scenarios, the latest IPCC reports, Special Report on warming of 1.5°C (SR1.5, Masson-Delmotte et al. 2018) and the Sixth Assessment Report (AR6, Masson-Delmotte et al. 2021), have extensively used global warming levels (GWLs, representing GSAT anomalies relative to the PI period; Cross-Chapter-Box 11.1 in Masson-Delmotte et al. 2018) as a new climate dimension for a better understanding and communication of what the future will look like, depending on the choices we make today. In this work, we provide a general overview on how global and regional SST and SSAT scale with global warming, based on a 26-member CMIP6 ensemble.

We specifically focus on the regional sensitivity of SST and SSAT to global warming across the IPCC AR6 reference regions (Iturbide et al. 2020) and ocean biomes, the two sets of regions applied in the latest IPCC AR6 report (Gutiérrez et al. 2021; Masson-Delmotte et al. 2021). Namely, we aim to investigate (1) how SST and SSAT scale with global warming on both global and regional scales, and (2) whether the results are robust to the SSP and the horizontal model resolution. Unlike for other atmospheric variables, such as extreme air temperature and precipitation (Seneviratne and Hauser 2020), sea temperatures appear to lack such comprehensive studies on regional scale.

Overall, this analysis provides information to assess the homogeneity of two different sets of regions in terms of regional response to global warming. This is relevant for a potential refinement of IPCC AR6 ocean reference regions, taking into account the spatial homogeneity in terms of regional response to global warming.

2 Data and methodology

2.1 CMIP6 GCM data and regionalization maps

We consider global monthly mean SSAT and SST from 26 CMIP6 GCMs (as listed in Table 1 in the Appendix) included in the IPCC working group 1 (WGI) Interactive Atlas (Gutiérrez et al. 2021). The selection of these GCMs was based on the availability of both SSAT and SST data for the historical experiment and four scenarios (SSP1-2.6, SSP2-4.5, SSP3-7.0 and SSP5-8.5) in the IPCC-WGI Atlas repository (Iturbide et al. 2020, 2021) or the Earth System Grid Federation (ESGF) at the time of the analysis. All data were interpolated from the original model grid to a common regular grid at a 1-degree horizontal resolution using first order conservative remapping (Jones 1999). To investigate the sensitivity of the results to the horizontal model resolution, we selected from the 26-member ensemble a GCM that pro-

vided versions with high and standard resolution over the ocean. The CNRM-CM6-1-HR and the lower resolution (LR) CNRM-CM6-1 (hereafter referred to as CNRM-CM6-1-LR, for clarity) models fulfilled the requirements. Their ocean fine and coarse nominal horizontal resolutions are 25 km and 100 km, respectively. For this sensitivity analysis, the datasets were interpolated to a common 0.25-degree regular grid.

We analyze regionally-aggregated results over the IPCC AR6 reference regions covering ocean areas, which include 12 oceanic and 3 mixed oceanic/terrestrial regions (Fig. 1, top panel). South-East Asia (SEA), the Caribbean (CAR), and the Mediterranean (MED) are those mixed regions, which are highly sensitive to climate change, MED particularly (Giorgi 2006). It is worth noting that the previous IPCC report (AR5) featured only three reference regions over oceans (Masson-Delmotte et al. 2013).

The regionalization in AR6 is mostly based on the ocean salinity trend analysis (Durack 2015), with additional regions covering the Southern Ocean (SOO) in the south and Arctic Ocean (ARO) in the North. Additionally, the equatorial regions are defined to capture the influence of specific phenomena, such as the El Niño or Indian Ocean Dipole effect. These new regions exclude coastal zones to a large extent. For that reason, we also include the regional analysis over ocean biomes (Fig. 1, bottom panel), which take coastal areas into account, allowing us to investigate how near-coastal processes, such as downwelling and upwelling, may affect the regional results. Both sets of regions are included in the Interactive Atlas (Gutiérrez et al. 2021) and the corresponding masks at different resolutions are available in the IPCC-WGI Atlas repository <https://github.com/IPCC-WGI/Atlas/tree/main/reference-regions>.

In addition to the regional assessment of the data, we analyze the grid-box by grid-box results. A comparison of grid-box to regionally aggregated data allows us to assess suitability of the two regionalizations for climate change analysis.

2.2 Scaling and GWL plots

We calculate decadal mean SSAT, SST, and GSAT anomalies relative to the 1850-1900 PI period. The mean anomalies are calculated independently for each of the 26 GCMs and 9 decades, from 2010 to 2100. Then we apply linear regression analysis using SciPy tool (Virtanen et al. 2020) to obtain the slope β of the linear fit of the mean decadal SST and SSAT anomalies to the corresponding GSAT anomalies (i.e. GWL). β is calculated following the expression:

$$\beta = \frac{N \sum xy - \sum x \sum y}{N \sum x^2 - (\sum x)^2}, \quad (1)$$

where x refers to data representing the mean SST or SSAT anomalies, and y corresponds to the dataset representing GWL. $N = 234$ represents number of individual data (26 GCMs \times 9 decades) per grid.

We examine the slope β of regional average anomalies in relation to GWL, serving as an indicator of the regional response of SST and SSAT to global warming. The results are presented in the form of a GWL plot, an extended version of the regional climate sensitivity plots (Seneviratne and Hauser 2020), as applied in the IPCC Interactive Atlas (Gutiérrez et al. 2021, <http://interactive-atlas.ipcc.ch>). The GWL plot is a scatter plot in which each point represents non-overlapping decadal mean anomalies of a target variable (SST and SSAT in this work) over a region of interest vs the corresponding GWL, over the same period relative to the reference PI period, calculated for each GCM. The GWL plot also includes the linear fit as applied in Diez-Sierra et al. (2023). Confidence limits for β are obtained by applying the commonly used two-sided Wald test with a 99% confidence (i.e. p-value below 0.01). Goodness of the fit is assessed by means of the coefficient of determination R^2 . Additionally, to identify cases in some regions where the scaling may be non-linear, we extend the GWL plot by including the curve of a fit to an exponential function ($y = Ae^{bx}$) using non-linear least squares.

2.3 Spatial plots

We also investigate the spatial distribution of the scaling factor by representing the regional scaling slopes on a map. The results are shown over the two sets of regions used in IPCC AR6 (Fig. 1). Furthermore, we calculated the β values for each grid cell to analyze the spatial consistency of the scaling at a finer scale. To distinguish the areas affected by sea-ice dynamics, on the gridded maps we also include information on sea-ice concentrations based on monthly mean sea-ice data available from the CMIP6 GCM simulations. We calculate the ensemble mean of the sea-ice concentration, and all areas where concentration is above 1% are considered as affected by the sea-ice dynamics and hatched on the gridded figures. The sensitivity of the slope β to horizontal resolution was calculated for each grid cell using the data from CNRM-CM6-1-HR and CNRM-CM6-1-LR GCMs. The information on sea-ice is included in the same manner as in the ensemble representation, but using just these 2 models instead of the full 26 model ensemble. We use the Pearson correlation coefficient to quantify the spatial similarity between the low- and high-resolution scaling patterns over different ocean biomes.

3 Results

3.1 GWL plots

Figure 2 shows an example of global and regional responses of SST and SSAT to global warming based on data from the SSP5-8.5 scenario, which provide the largest range of global warming during the 21st century.

Both SST and SSAT scale linearly with GWL on the global scale (Fig. 2ab). As expected, their scaling factor is lower than 1, meaning that both temperatures scale with global warming, but at a lower pace. SSAT scales with a factor of 0.86 K/K, so e.g. SSAT over oceans responds with +3.4 K to a +4 K GWL. For SST the slope is 0.71 K/K, i.e. a +2.84 K response to the +4 K GWL.

On the regional scale over the IPCC regions, SST scales linearly with a scaling factor β ranging between 0.7 and 0.85 K/K for most of the regions (see Fig. 10 in the Appendix). Lower β values are obtained over most SH regions (i.e. SAO, SOO, SPO), with the lowest value of 0.54 over SOO. The latter is related to the presence of sea-ice in the area, since most of the energy is spent in the phase change between sea-ice and sea-water instead of heating (Armour et al. 2016; Haumann et al. 2020). Sea-ice is projected to start to decline in the second half of the 21st century (Rackow et al. 2022), which is one of the main reasons for SST in the area to rise significantly slower than in the rest of the IPCC regions. However, a different behavior can be observed in the Arctic Ocean (ARO). ARO exhibits the highest β for SST among all the IPCC regions (Fig. 10 in the Appendix). However, it also displays the highest inter-model spread (Fig. 2c), resulting in very similar R^2 values for both the linear (0.70) and exponential (0.71) fits. This behavior, in contrast to SH, is attributed to the faster melting of sea-ice in NH (Masson-Delmotte et al. 2021; Rantanen et al. 2022). Once sea-ice has melted, SST rises more rapidly with GWL due to changes in albedo and sea-atmosphere feedback. Discrepancies in the representation of sea-ice melting contribute to a higher inter-model spread in the results, particularly at higher GWLs. This difference is also evident in the standard error, which is at least twice the value of those obtained in the other IPCC regions (i.e. 0.013 K/K, Fig. 10 in the Appendix). The coupling between SST and SSAT in this region strongly depends on the way the behavior of sea-ice is parametrized in the model, and the CMIP6 models use different sea-ice parameterization schemes to represent sea-ice sub-grid scale processes (see Table 1 in the Appendix), leading to a higher spread in sea-ice extent (Long et al. 2021). These differences in sea-ice extent affect the spread of β between SST and GWL in this region (Fig. 2c). In the neighbouring North Atlantic Ocean

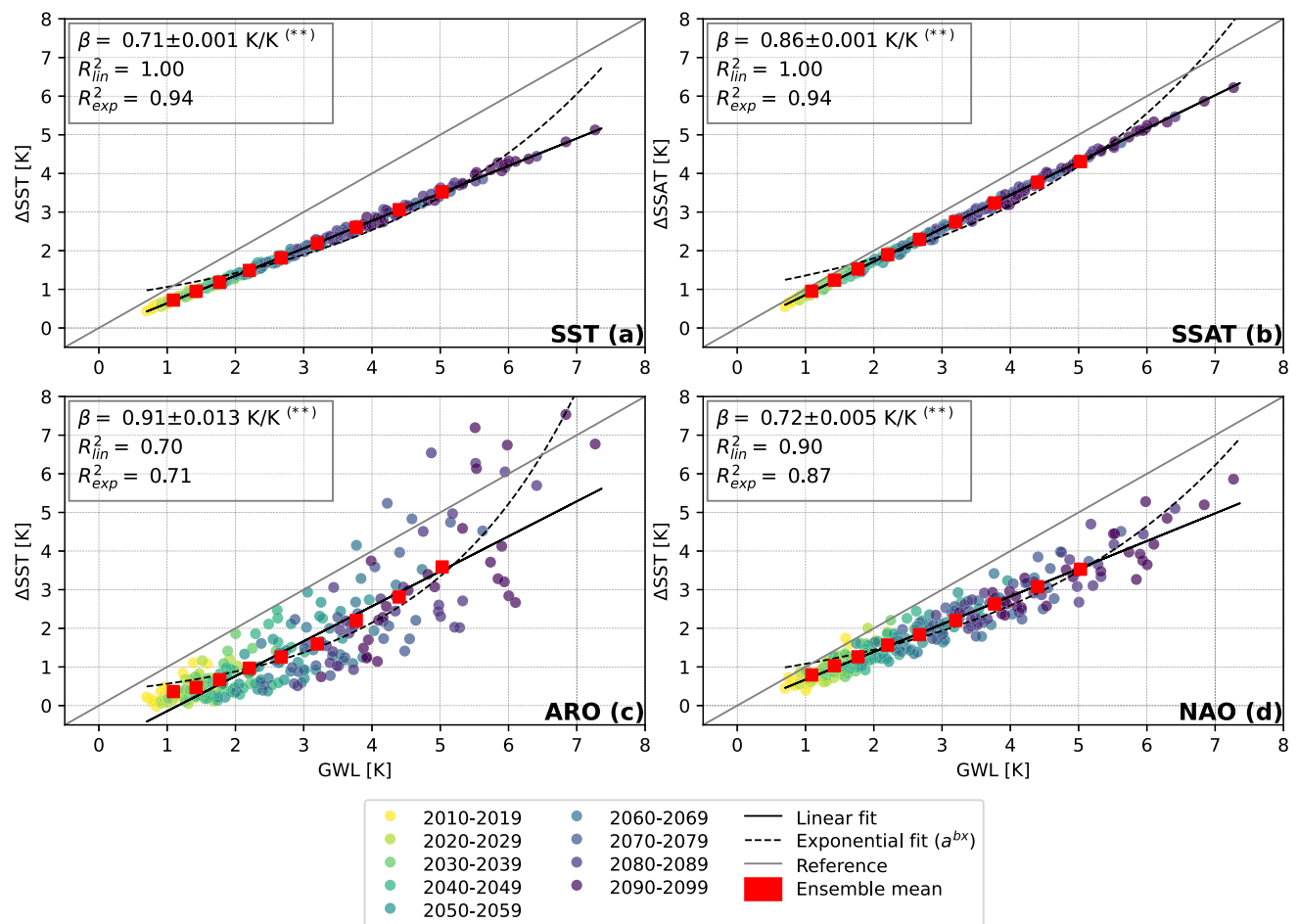


Fig. 2 Global Warming Level (GWL) plots showing the responses of global (a) SST and (b) SSAT to global warming, as well as two examples of regional responses of SST to global warming over two IPCC regions: (c) Arctic Ocean (ARO), and (d) North Atlantic Ocean (NAO). Filled dots represent mean decadal anomaly for each of 26 GCMs since during the 21st century with respect to the baseline PI period (1850-

1900). In the upper left corner statistical information on the slope β with asterisks indicating the significance level based on the p value (** for $p \leq 0.01$), the coefficient of determination R_{lin}^2 of the linear fit (black solid line), and R_{exp}^2 of the exponential fit (black dashed curves). Red squares represent the decadal ensemble mean values

(NAO) region, which is sea-ice free, SST scales linearly with GWL (Fig. 2d), showing a good linear fit ($R_{lin}^2 = 0.90$), and much smaller spread.

The scaling of SSAT with GWL over the IPCC regions (Fig. 11 in the Appendix) shows that only ARO warms faster than mean GSAT, and MED is almost as fast. SSAT over MED scales with, $\beta = 0.95 \pm 0.005 \text{ K/K}$, while over ARO SSAT has a tendency to rise almost three times faster than the global average ($\beta = 2.98 \pm 0.020 \text{ K/K}$). The latter is lower than the four times faster increase reported by Rantanen et al. (2022). The reduced rate we obtained is attributed to our analysis procedure, which incorporates regions covered by sea-ice. Over these areas the SSAT increase is limited by the sea-ice layer. Results are robust on both global and regional scales for all analyzed IPCC reference regions (red squares representing the ensemble mean on Fig. 2, as well as Figs. 10 and 11 in the Appendix).

To test the sensitivity of the scaling factors to the emission scenario, we computed annual and seasonal scaling factors β of SST with GWL, on both regional and global scales for all SSPs (see Fig. 12 in the Appendix). On the global scale, the annual and seasonal β results for SST are robust, with variations below 3% depending on the scenario, and with small differences between seasons. On the regional scale, seasonal differences for different SSPs differ up to 10%, typically reaching the highest β for the high-emission SSP5-8.5 scenario. In SOO and NAO, β is the highest for SSP1-2.6 in winter and spring, as well as for MED but only annually. Furthermore, for ARO, NAO, NPO, and MED, seasonal variations are evident, with differences above 10% (in ARO the β values are more than doubled when going from DJF and MAM to JJA and SON).

Global β variations for SSAT with SSP (Fig. 13 in the Appendix) are up to 5%, showing no large differences

between seasons. On the regional scale, the differences between the SSPs do not exceed 10% in most cases, except in the sea-ice regions. In the case of SSAT the highest β for SSP1-2.6 appear in ARO and SOO, with large differences between seasons for all SSPs in MED, NPO, SOO and, especially, in the ARO region. In this region, the highest β values for SSAT are in SON and DJF (4.78 to 6.41 K/K, depending on the SSP) and the lowest in JJA (1.22 to 1.32 K/K), which is related to seasonal changes in the sea-ice concentration. During fall and winter, most of the solar radiation is reflected due to the high sea-ice albedo, and the SSAT increases faster. In summer, the melted sea-ice allows for the solar radiation to be absorbed by the sea, and therefore the increase of SST with global warming is the highest, and the increase of SSAT the lowest (Levine et al. 2021).

3.2 Regional responses to global warming

Figure 3 represents β spatially for the 26-member CMIP6 ensemble mean annual and seasonal regional responses to GWL for the SSP5-8.5 scenario. The results are calculated over the IPCC reference regions, biomes regions, and per grid cell for both SST and SSAT. Responses for SST are higher in the NH than in the SH, as expected (Masson-Delmotte et al. 2021; Ruela et al. 2020). Furthermore, there is a northward positive gradient of intensity of β for SST, especially during JJA and SON. The scaling factor in SH does not exceed 0.75 K/K throughout the whole year, while in NH this value is exceeded in most of the regions, especially during JJA and SON in the ARO and MED IPCC reference regions, as well as in NH High Latitudes (NHHL) and MED biomes regions, where SST is predicted to increase faster than the global warming under SSP5-8.5 (i.e. $\beta > 1$ K/K).

Gridded maps (Fig. 3, third row) show small scale features that can be distinguished especially in upwelling regions and areas of strong ocean currents. In the regions of the Canary, Humboldt, and South Indian currents, there is a very weak response of SST to global warming, with β below 0.5 K/K during all seasons. Extremely low and also negative values during DJF and MAM can be distinguished within the NHHL biome, southeast from Greenland, indicating cooling of SST. This coincides with the warming hole where cooling has already been observed and often related to the weakening of the Atlantic meridional overturning circulation (AMOC; Medhaug et al. 2017; Caesar et al. 2021; Keil et al. 2020). The results indicate that the SST cooling in this subregion is projected to continue. On the other hand, the Equatorial counter current within the EO biome, a region strongly affected by ENSO, shows responses mostly greater than 1 K/K, indicating that SST warms there faster than the GSAT. Additional

features with stronger response to global warming can be distinguished south of Australia, which may be related to seasonal upwelling, and in the Argentine Sea just outside the mouth of the La Plata river.

The response of SSAT to global warming is similar to SST, for most of the equatorial and midlatitude regions; it is substantially different only for the regions with permanent sea-ice. The increase of SSAT over ARO regions is projected to be 3 to 6.5 times faster than the GSAT, depending on the season, with the highest values (6.5 K/K) in DJF. The latter is also evident over corresponding biome regions, as well as in the gridded representation. On the other hand, the gridded representation of the SSAT response to global warming adds on the regional information over SOO. Close to the Antarctic coast, SSAT is projected to increase much faster than in the rest of the SOO region or SHHL biome, which is clearly related to the presence of sea-ice (hatched areas in Fig. 3).

There is a clear consistency between these two regional aggregations of the slopes for the SOO and SHHL regions, but the spatial aggregation is the result of compensating slopes in the southern Pacific and along the Antarctic coast, which can be distinguished in the grid-box by grid-box assessment. The loss of information due to compensating slopes of β can be also seen in the SAO reference region. In the NH biomes (i.e. NHS and NHHL) and the SHS region covering the northern part of the Indian Ocean, the consistency between the two regionalizations is less evident as well, with strong gradients of the slopes in their gridded representation. These biome regions include three IPCC reference regions - NAO, NPO and EIO. The strongest slope gradients for both temperatures appear in NAO, where the effects of the warming hole are compensated with the high slopes along the eastern Canadian coast (Fig. 3, rows 3 and 6). There are β differences of up to 40% between the northern and southern parts of NPO in the gridded representation (especially for SST) and over the two neighboring ocean biome regions (NHHL and NHS), but they are compensated in the regional representation over the IPCC regions. Furthermore, the effects of seasonal upwelling on β for SST in the Arabian Sea (AS) is visible in the gridded representation during DJF and MAM, which is not evident in the EIO IPCC reference region. Furthermore, it is interesting to note that the biomes covering coastal regions, such as EB and AR, are excluded from the IPCC ocean regions and merged into the continental reference regions. On the other hand, the gridded slopes show that there are only small discrepancies over oceanic coastal biomes as compared to their surrounding regions.

These results suggest that certain oceanic IPCC AR6 reference regions may be redefined in order to better capture the spatial variability of regional sensitivity to climate change.

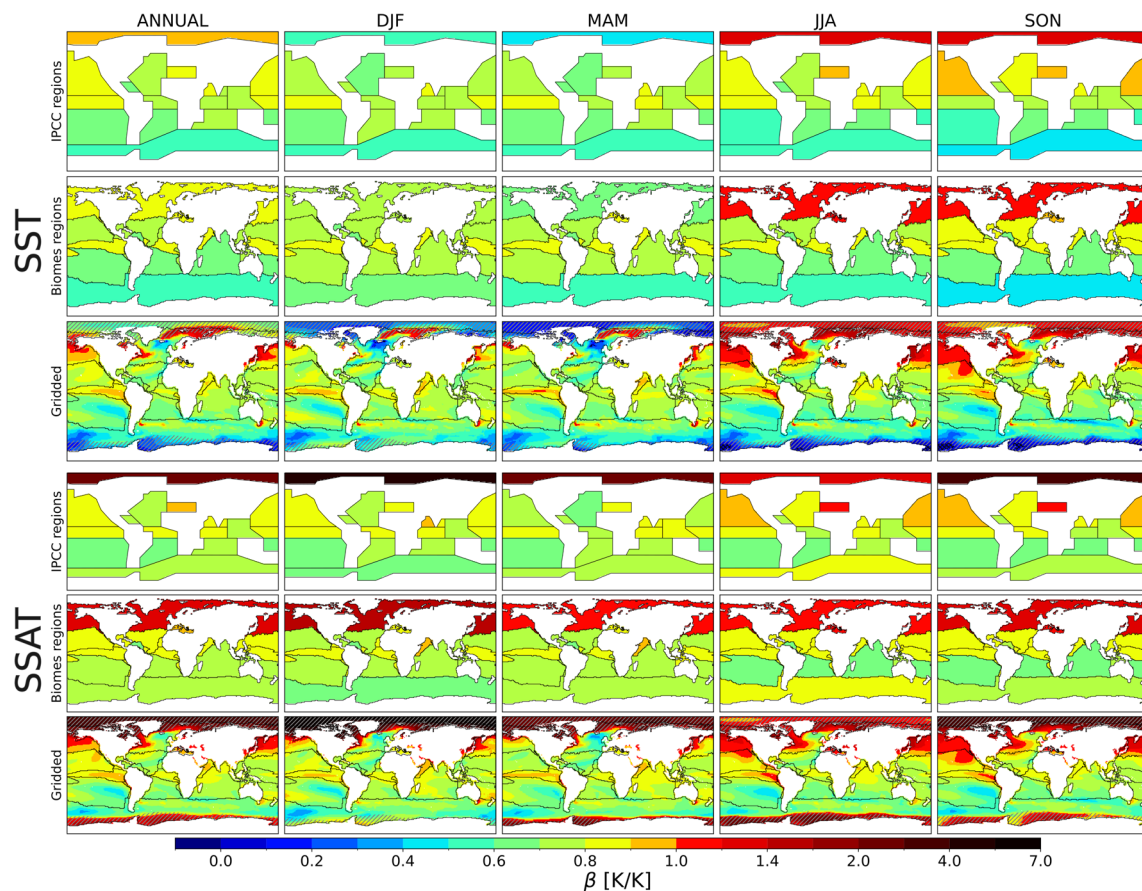


Fig. 3 Annual and seasonal (columns) slope β [K/K] of the linear scaling of SST (top 3 rows), and SSAT (bottom 3 rows) with global warming for the SSP5-8.5 scenario, over IPCC reference regions (1st and 4th row), biomes (2nd and 5th rows), and each grid cell (3rd and 6th). Hatched areas indicate the areas where the sea-ice concentration

exceeds 1% (single hatching patterns), and black crosshatched areas indicates the areas with non-significant results. Biomes region boundaries are overlaid on the gridded plots to facilitate visual analysis of regional consistency

In the same manner, SOO and NPO show a strong gradient towards the equator, and according to the gridded results, the regions should be subdivided in two subregions. In SAO, a strong feature in the Argentine Sea outside La Plata river's mouth can be clearly distinguished, indicating a potential subdivision of the region in two parts as well. Strong contrasting features in NAO, including the effects of the warming hole, suggest the subdivision of the region in three parts, while ARS region could be extended by incorporating a portion of the Equatorial Indian Ocean (EIO), to better capture the effects of seasonal upwelling in the AS biome. A refinement of the IPCC reference regions over oceans according to these suggestions is illustrated in Fig. 4.

To illustrate the application of these proposed regions, we show (Fig. 5) the spatial spread of β for SST (for SSAT in Fig. 15 in the Appendix) within both the current six IPCC AR6 regions that were refined and the newly suggested ones. The results highlight variations in the spatial distribution of β for the newly defined regions, particularly noticeable in NAO.

Sub-regions within NAO, such as SNAO, exhibit a more homogeneous spatial β distribution as compared to EANO and WCNAO, with the latter two differing in their mean value. Pronounced differences in spatial spread of β can be seen in NPO and SOO, where regions more impacted by sea-ice (NNPO and the new SSO) display a higher spread. The SAO region exhibits high seasonal sensitivity, evidenced by a substantial difference in spread between the two newly proposed regions during JJA. The newly proposed ARS region mostly features a significantly higher spatial spread, while this change does not have a strong impact on the newly proposed EIO.

3.3 Sensitivity to the GCM horizontal resolution

The analysis presented in the previous section considered an ensemble of GCMs, combining various models with different grid spacings, and the gridded results (Fig. 3, rows 3 and 6) showed details related to specific ocean features such

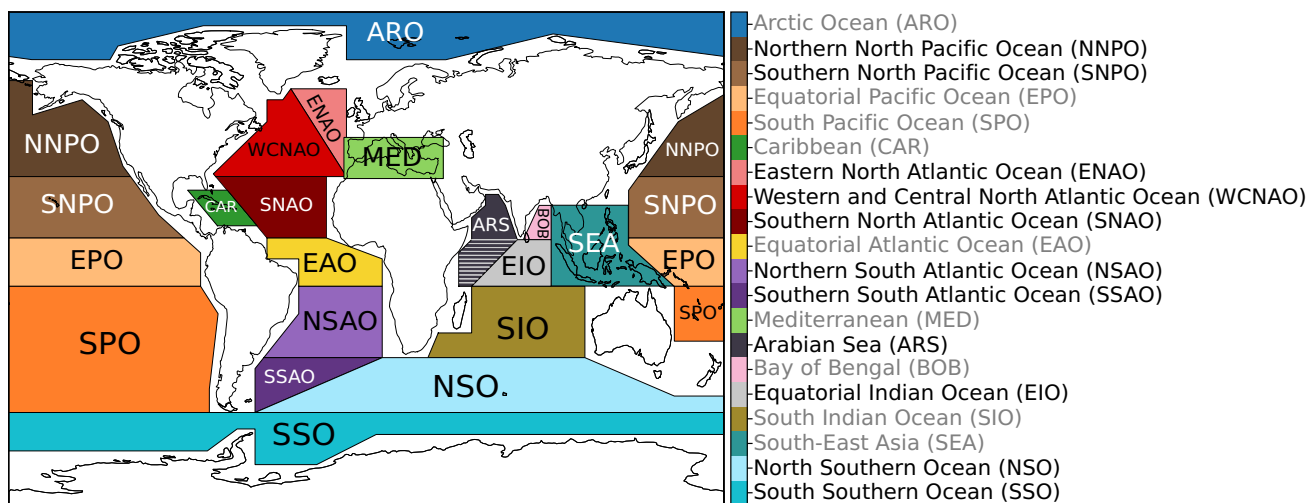


Fig. 4 Suggested refinement of the IPCC ocean reference regions (region names in bold). NPO, NAO, SAO and SOO are divided in two subregions, NAO in three subregions. EIO is split in two subregions, with the left part (striped) merged to ARS

as upwelling regions or presence of strong currents. In this section, we analyze the robustness of the above results with respect to horizontal resolution by performing the analysis on two individual GCMs that differ only in their grid spacing.

Figure 6 shows the grid cell scaling of the CNRM-CM6-1-HR model, which has the highest resolution (HR) over the ocean areas (25 km) among the 26 ensemble members, and

the comparison to the results from the corresponding CNRM-CM6-1-LR GCM at lower resolution (100 km), and the difference between the two. The highest differences between LR and HR can be seen again in the regions with the influence of the sea-ice dynamics (hatched areas in Fig. 6), especially in the region covering the Southern Ocean (i.e. SHHL) in austral summer (DJF) and autumn (MAM), which show a

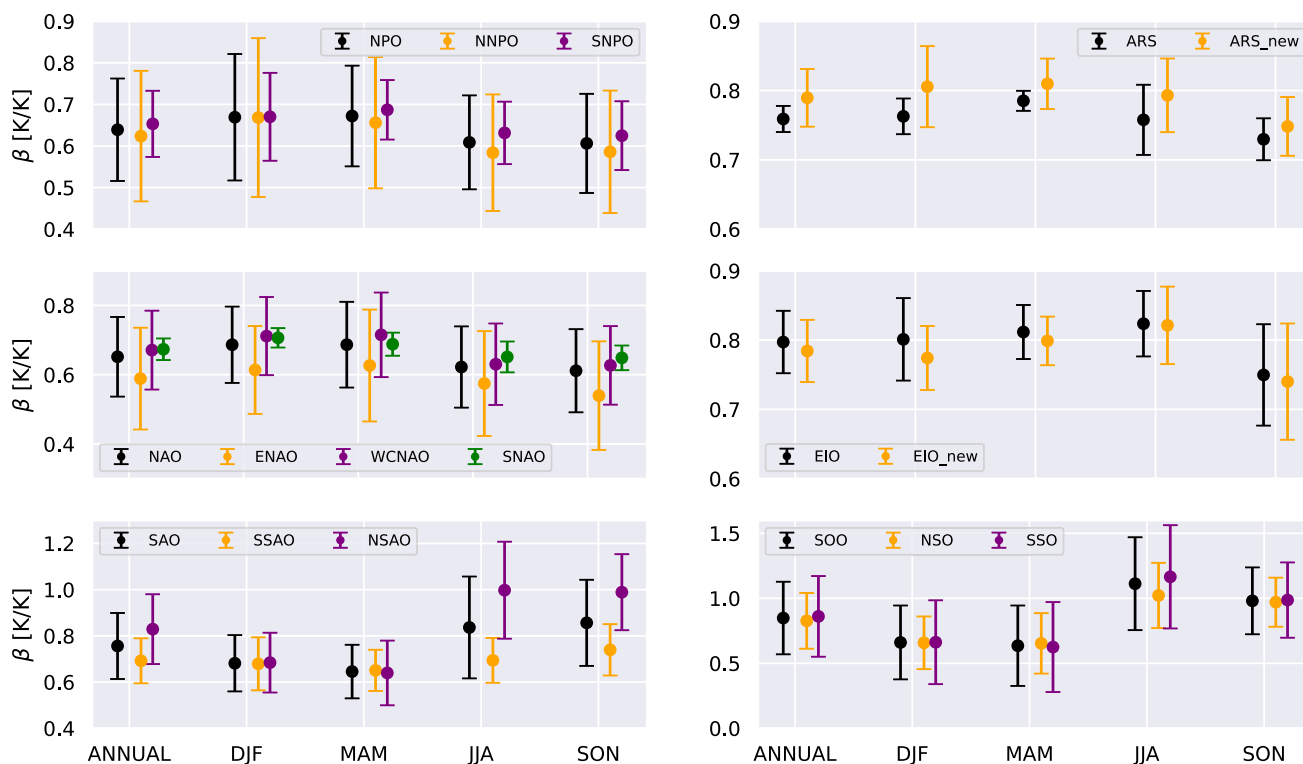


Fig. 5 Spatial mean and spread of β for SST. The results are displayed for both the six existing IPCC AR6 regions (one region per panel, black markers) and their newly suggested counterparts (in colors, see legend)

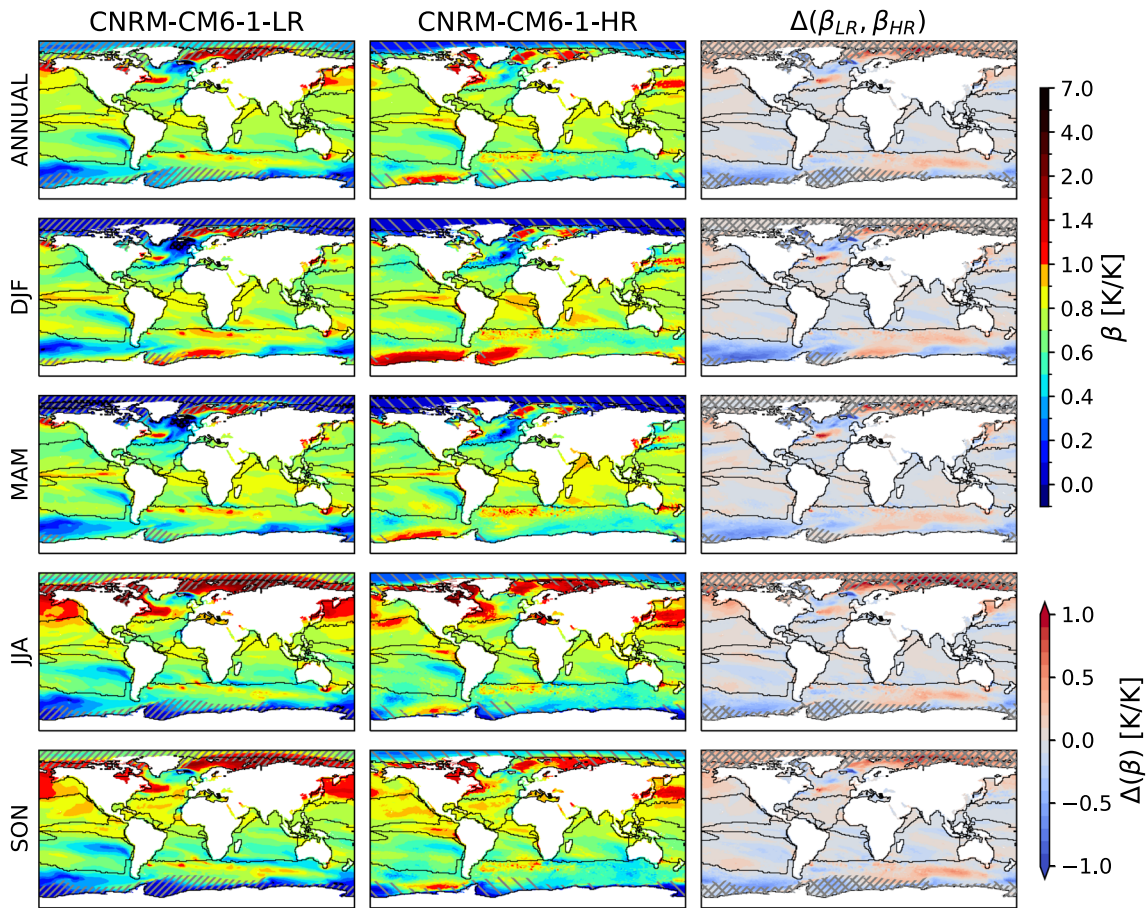


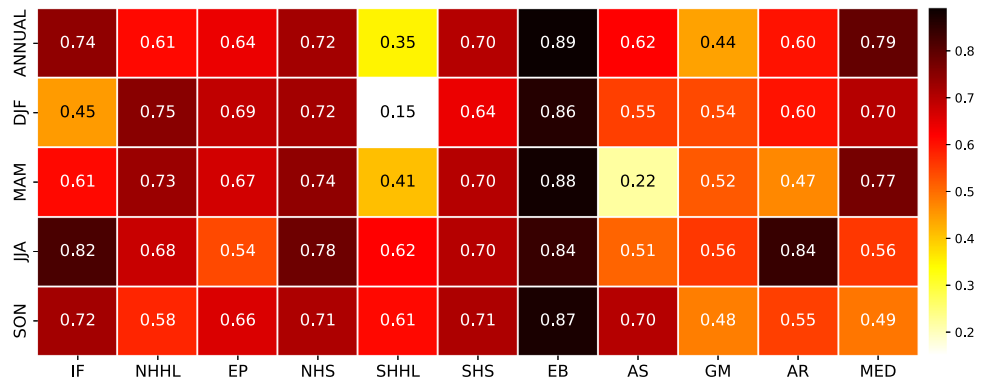
Fig. 6 Annual and seasonal (rows) representations of the β slope for SST in [K/K] calculated for each grid cell, all interpolated at 0.25 regular grid for the CNRM-CM6-1-LR (1st column), CNRM-CM6-1-HR (2nd column), and the difference between the two (3rd column). Overlaid

black lines indicate ocean biomes boundaries. Hatched areas show the areas with sea-ice concentration above 1% (single hatching patterns). The areas with non-significant results use the crosshatched in black

spatial correlation coefficient $R < 0.5$ (Fig. 7). Overall, the mean area covered with sea-ice is larger in the LR simulations in the south, while in the north more sea-ice is simulated with the HR model. More pronounced local features can be distinguished in the LR simulations. For example, the features in the Argentine Sea and southern Australia, also visible in the ensemble mean (Fig. 3), can be clearly distinguished in

the LR, but not in the HR simulations (e.g. see Fig. 15 in the Appendix), where the features seem to be smoothed. Furthermore, some features such as in the ocean area east from Peru, eastern and western edges of the SHHL region, and in south from the Indian Ocean, are smoother when increasing the model resolution. This can be related to the stronger deep water mixing which is simulated in the higher resolution

Fig. 7 Spatial correlation R coefficient calculated as the Pearson coefficient between the slopes β from the 2 sets of data, CNRM-CM6-1-LR and CNRM-CM6-1-HR, over the grid cells included in each of the 10 ocean biomes



ocean models (Koenigk et al. 2021). This causes more efficient water transport northwards in the SH and southwards in the NH in the HR simulations, which might smoothen the gradients that are visible in the LR run.

From a regional perspective, regions with seasonal upwelling, such as the Arabian Sea (AS), Gulf of Mexico (GF), and Amazon River (AR), show the lowest spatial correlation between the two resolutions, with R values around or below 0.5 (Fig. 7). On the other hand, the area covering EB, the regions with prominent continuous upwelling processes along the coast, show the highest spatial correlation between LR and HR models. Within the EB region, slightly higher differences can be seen only in parts of the Humboldt upwelling system (see Fig. 6).

The Mediterranean area has been identified as a hotspot of climate change (Giorgi 2006). In Fig. 8, we focus over the MED biome (the Mediterranean Sea). The differences in the spatial pattern between the 2 resolutions are the highest in JJA and SON seasons. In JJA, the HR model version for most parts, especially over Tyrrhenian, Ionian, and Balearic Seas, accounts for faster SST warming than the mean GSAT in JJA (i.e. $\beta > 1$), which is not the case for the LR version. In most of the biome, the HR version of the model account for higher values of β than its corresponding LR version, with an exception in the Gulfs of Lyon and Gabes, where slightly higher values are obtained with LR, especially in DJF season. The spatial correlation is the lowest in JJA and especially in SON season, when the HR version accounts for more than 20% higher values in the Adriatic and Ionian seas.

NHHL also shows a distinct behavior due to the presence of the North Atlantic warming hole. Figure 9 represents the part of NHHL covering the NAO IPCC reference region. Different local patterns can be distinguished in the LR results, which are completely absent in the HR version, especially during DJF and MAM. The area with β above 1 K/K in the LR version does not appear in the HR model. The strong gradients that are evident in the LR model are much smoother in

the HR model version. Furthermore the location of minimum negative β values, indicating the location of the warming hole, are shifted eastward from the location in the LR model version. Note that these areas with minimal values are not significant. It is known that HR models tend to simulate stronger mixing, especially in subpolar gyres (Koenigk et al. 2021), and that AMOC is projected to weaken more in the future when the model resolution is increased (Roberts et al. 2020). The results depicted in Fig. 9 are consistent with these findings, where the gradients are significantly smoothened due to the increased mixing in the HR model version, and better represented southward water transport (Chassignet et al. 2020, 2017). Furthermore, the difference in amount of sea-ice between the two simulations affects the sea-ice-albedo feedbacks, which may strongly affect sea-ice seasonal shifting and, consequently, the presence of sea-ice in the selected region (Kashiwase et al. 2017).

4 Discussion

Both SSAT and SST scale linearly with GWL on a global spatial scale, with annual scaling factors 0.86 ± 0.001 K/K and 0.71 ± 0.001 K/K respectively, with slightly higher values in JJA and SON. On the regional scale, most regions scale linearly as well with GWL, but with very different scaling factors. Regions in SH have notably lower values than the regions in the NH, indicating that the oceans in NH are projected to warm faster than those in the SH, which is in agreement with Ruela et al. (2020). The lowest annual value of $\beta = 0.54 \pm 0.005$ K/K for SSP5-8.5 is obtained over the SOO region, indicating that this part of the globe will warm at the slowest annual rate, with almost no changes between the seasons. Conversely, the region with the highest annual value of $\beta = 0.91 \pm 0.013$ K/K among the IPCC reference regions is ARO. The annual scaling of SST with GWL in this region fits slightly better to an exponential model, suggesting that

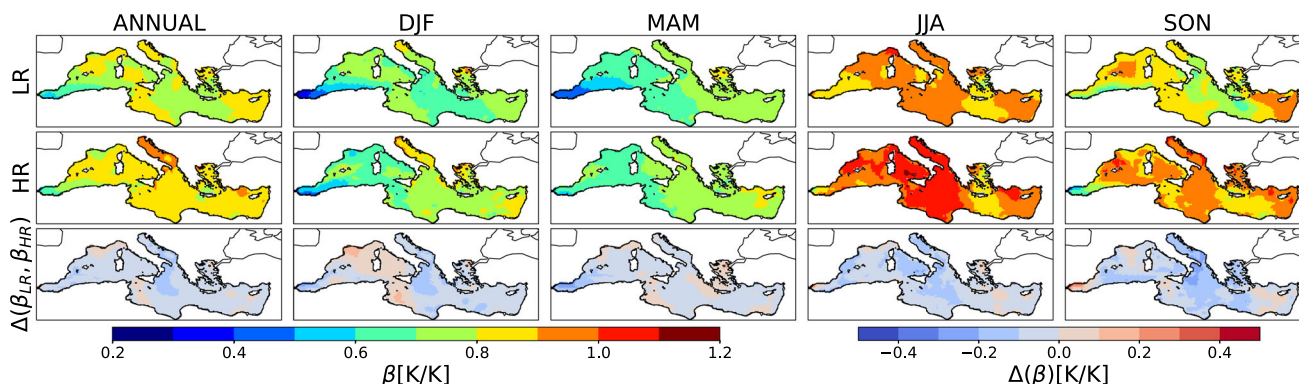


Fig. 8 As Fig. 6, just zoomed over the Mediterranean region (MED)

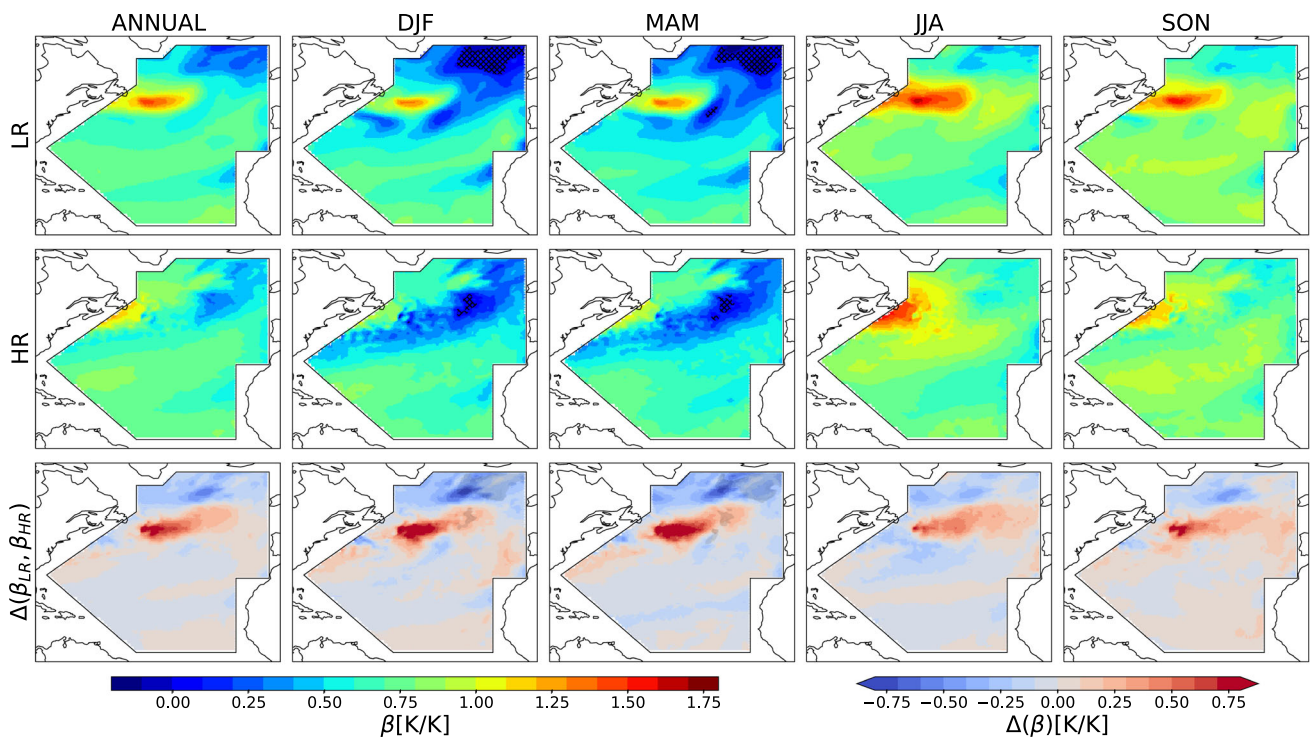


Fig. 9 As Fig. 6, just zoomed in over the North-Atlantic Ocean (NAO) IPCC reference region. Crosshatched areas are not significant according to a two-sided Wald test with a 99% confidence

the increase of SST accelerates as higher GWLs are reached. The ensemble spread of β is high in ARO (i.e. β differences between the CMIP6 GCMs), with the standard deviation of an order of magnitude higher than in the rest of the regions. ARO also shows a strong variation of β between the seasons, with β well above 1 K/K in JJA and SON, and very low values ($\beta \sim 0.5$ K/K) in DJF and MAM. Such behavior in the polar regions can be explained by the presence of permanent sea-ice, which represents a blocking barrier for solar radiation (i.e. reflects due to high albedo) and therefore limits the increase of SST. Sea-ice melts much faster in ARO than in SOO, and it is projected to start to disappear completely during JJA season by the mid 21st century (Gutiérrez et al. 2021; Masson-Delmotte et al. 2021). Therefore, a strong differences of β between the seasons are evident in this region, with significantly higher β values in JJA and SON, in the seasons when the sea-ice in the region is minimal or even absent. On the other hand, in DJF and MAM, before sea-ice is melted, the scaling factor β is very low. In this region, the change of β between the seasons for SSAT is reversed; it is the lowest in JJA ($\beta = 1.32$ K/K) and the highest in DJF ($\beta = 4.78$ K/K). However, in the south, there are no strong seasonal variations, as sea ice melts there at a slower rate than in the north. For that reason, β is the lowest in SOO with the changes

between the seasons not as evident as in the northern sea-ice regions.

The spatial representation of β at grid cell scale shows additional features and details. For example, in the NAO region, the location of the warming hole can be clearly distinguished, which is masked in the regional analysis. This location of extremely low and negative β shows that the negative trend will persist in DJF and MAM season. Extremely low values can be distinguished also in subregions of SOO, which coincides with the regions having currently negative SST trends (Armour et al. 2016; Auger et al. 2021; Xu et al. 2022). The results in this study indicate that these negative trends in the SOO region tend to change the sign in the future at highest GWL. Furthermore the gridded representation of β allows to easily distinguish the Equatorial counter current within the EO biome having $\beta > 1$, indicating that the SST in this region will increase faster than the mean GSAT. Locations south of Australia and in the Argentine Sea, just outside the La Plata river's mouth, also show faster SST warming than the mean GSAT. In general, the SST pattern follows that of SSAT, except for the regions influenced by sea-ice dynamics, especially when focused on the changes between the seasons. In the sea-ice regions in both hemispheres the summer SSAT scaling is the lowest, while in winter it is the highest.

The sensitivity to the GCM's horizontal resolution was analyzed by comparing the gridded representation of β using the same GCM on 2 different resolutions. The main difference between the two representations is not in the overall patterns represented, but in the fact that the same features in the HR model version are smoothed when compared to the representation given by the LR model. This is especially evident in the regions with the special features, such as in NHHL around the warming hole, and in the whole SHHL biome, where the differences in β tend to be higher than 50%. The reason for these large differences in SHHL can be related to the stronger mixing of the ocean waters and more efficient transport towards the North, which is characteristic for the HR models in general (Koenigk et al. 2021). In the warming hole, it may be related to AMOC, which is projected to weaken more in the future when the model resolution is increased (Roberts et al. 2020).

From the 3 mixed regions, in SEA and CAR linear scaling of β is evident for both SST and SSAT, with a small spread between the models (Figs. 10 and 11), and small interseasonal variability (Figs. 12 and 13). Distinctive scaling characteristics of β with GWL are evident only in MED. SST and SSAT scales linearly with GWL also in this region, but the values for β (0.85 ± 0.005 K/K and 0.95 ± 0.005 K/K, respectively) are notably higher than in most of the analyzed regions. Furthermore, seasonal variations are evident, with differences of up to 20% between the seasons. In summer the SSAT increase is projected to be even faster than the global warming ($\beta = 1.08 \pm 0.005$ K/K). This region also shows a sensitivity to the resolution, as it includes a very complex coast, and HR models tend to better resolve the orography and sea-land discontinuities. The HR model overall gives the higher SST-GWL scaling factors than the LR model version, with the highest difference in summer and autumn seasons.

5 Conclusions

In this study we investigate the response of SST and SSAT to global warming using the latest CMIP6 GCM simulations. The analysis is focused on these two variables, with GWL used as a dimension of global warming. We analyze

SSAT, which is obtained from GSAT by masking the land surface. For each variable, we calculate non-overlapping 10-year mean anomalies with respect to a PI period, and we analyze how SST and SSAT scale with the corresponding GSAT anomalies, which is a specific form of the GWL representation. We analyze the slope β of the linear fit on global and regional spatial scales, as well as on annual and seasonal temporal scales. Additionally, we applied a one-term exponential model to analyze if and how the fitting depends on the region and season. We applied 2 types of regionalization, i.e. over the IPCC reference regions and ocean biomes (Gutiérrez et al. 2021; Masson-Delmotte et al. 2021; Iturbide et al. 2021), as well as the grid-box per grid-box analysis, to investigate whether the results are robust to the type of the regionalization applied.

The application of the linear regression method to assess the scaling of SST and SSAT with GWL unveiled strong differences in the results at the regional scale. Further examination of the linear scaling factor β at the grid scale provided more detailed insights into oceanic features and potential inhomogeneities within the same region. The pronounced gradients identified in the gridded β within IPCC AR6 reference regions indicate the need to enhance the borders of specific ocean regions in forthcoming regional climate change assessments. Particularly affected regions are the Southern Ocean (SOO) and South Atlantic Ocean (SAO) regions in the Southern Hemisphere, along with the North Atlantic Ocean (NAO), North Pacific Ocean (NPO), and Equatorial Indian Ocean (EIO) regions in the Northern Hemisphere. A redefinition is necessary to account for the effects of local features specific to each region. We propose incorporating five additional oceanic regions to complement the existing twelve IPCC reference regions over oceans (Fig. 4). Moreover, with an anticipated increase in the horizontal resolution of GCMs, coastal areas are expected to be better resolved. These coastal areas predominantly constitute parts of the continental regions in the current version of the IPCC reference regions, as illustrated in Fig. 1, where a noticeable gap exists between the borders of the ocean regions and coastlines. It will be crucial to refine the ocean regions further to incorporate these coastal areas, to enhance the accuracy of future regional climate assessments.

Appendix: Additional figures and tables

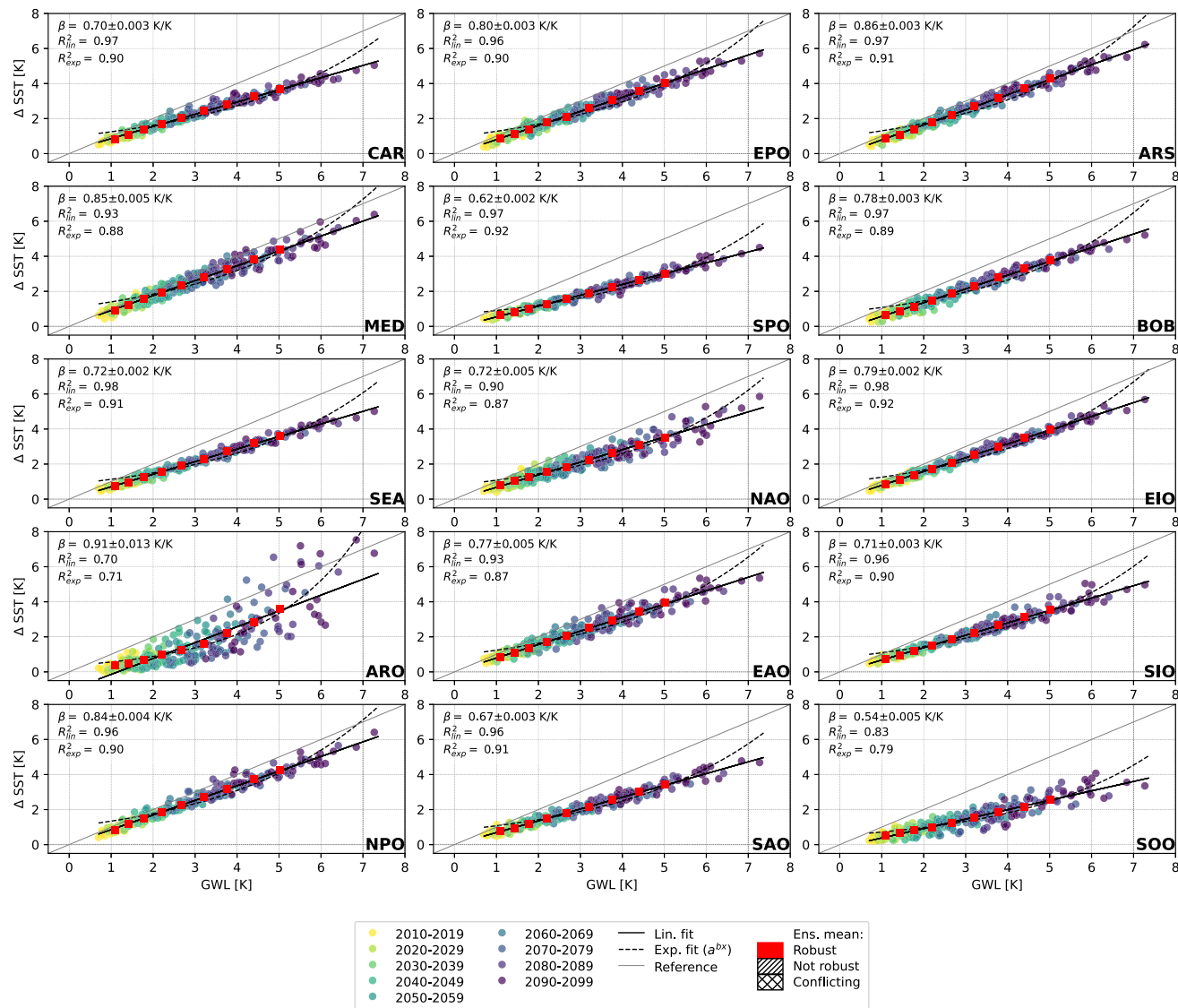


Fig. 10 GWL plots showing responses of regional SST to global warming over the IPCC reference regions. Filled dots represent mean decadal anomaly for each of the 26 GCMs during the 21st century since 2010 with respect to the baseline period (i.e. 1850-1900). In the upper left corner statistical information on the slope β and the correlation coefficient

R_{lin}^2 of the linear fit (black solid line), and R_{exp}^2 of the exponential fit (black dashed curves). Squares represent the decadal ensemble mean values, including information on the robustness over the 21st century (all shown in red i.e. all robust)

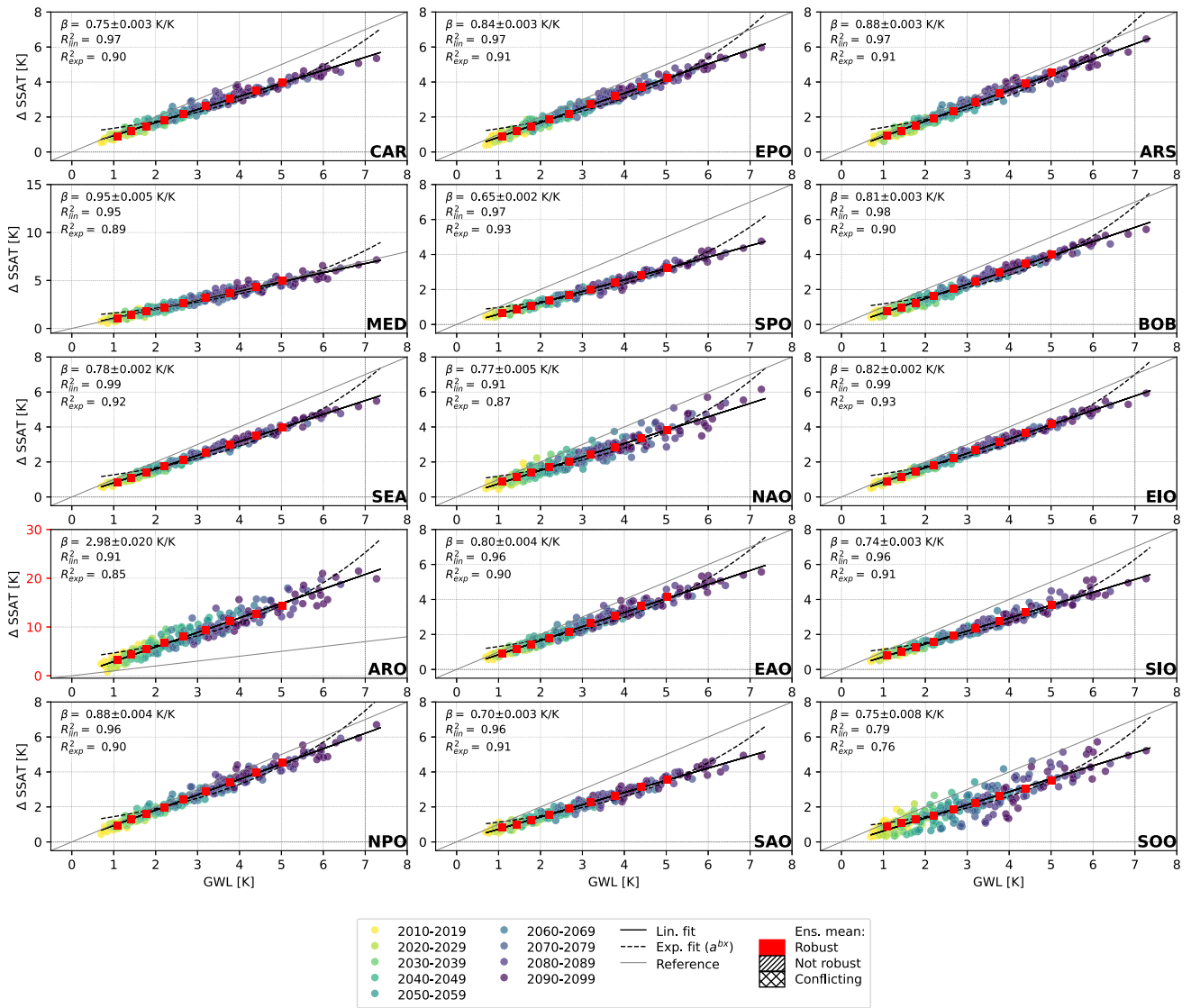


Fig. 11 As Fig. 10 but for SSAT

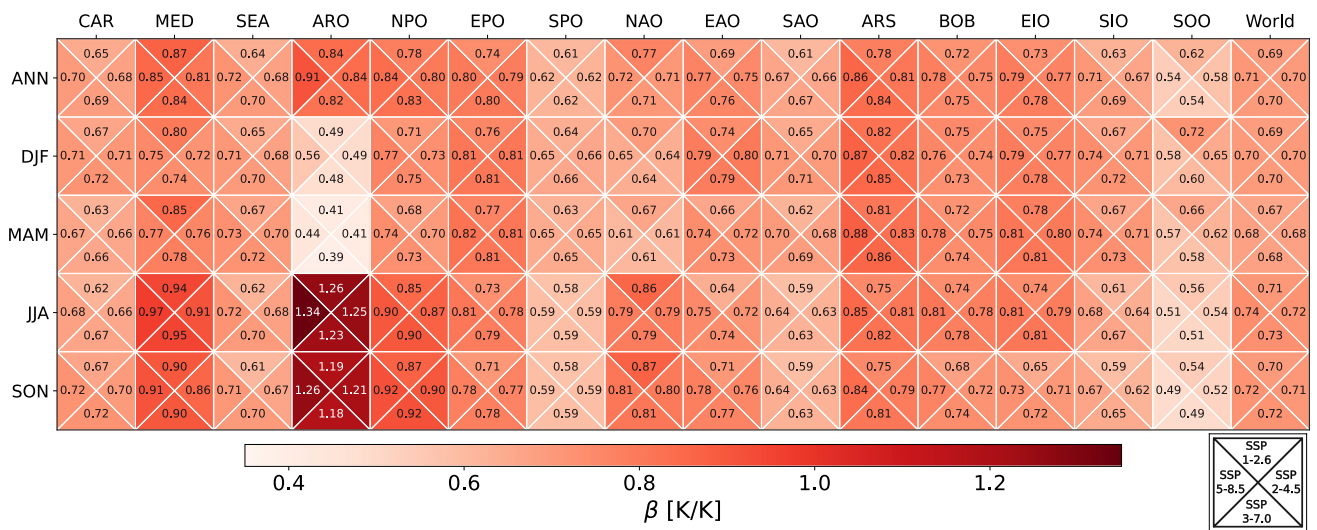


Fig. 12 Heat map of annual and seasonal β between SST and GWL in K/K units (rows) over the IPCC regions (columns) and globe (last column), for 4 SSPs (triangles)

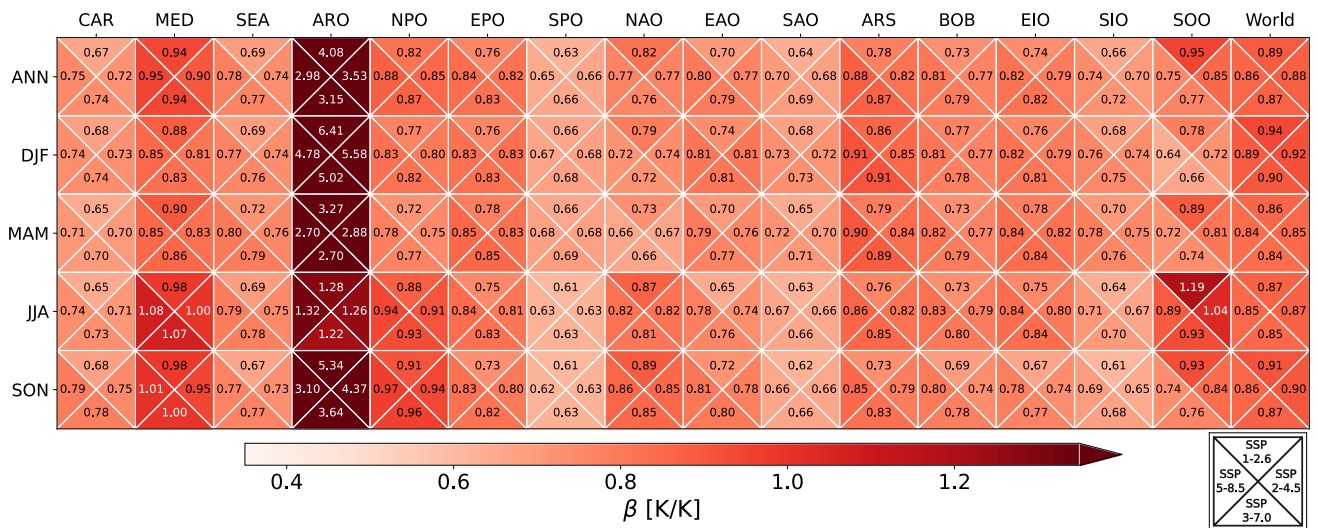


Fig. 13 As Fig. 12 but for SSAT

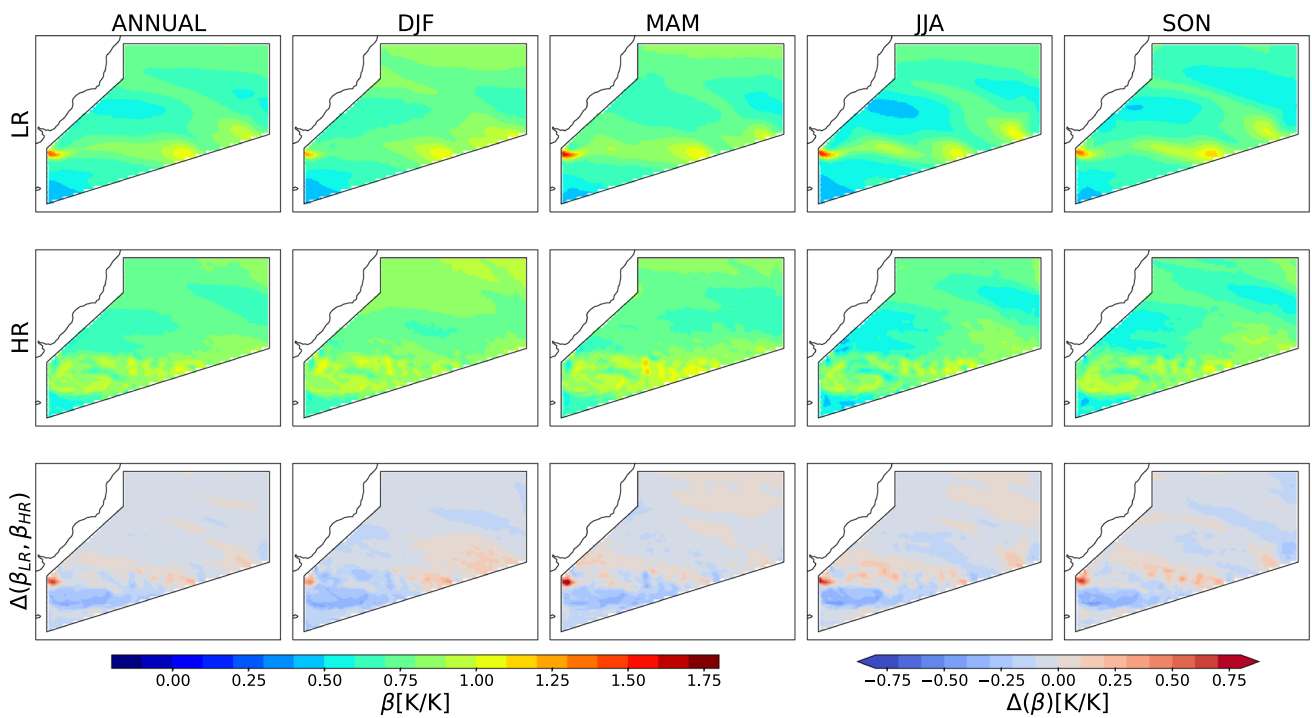


Fig. 14 Annual and seasonal (columns) representations of the β slope for SST in [K/K], zoomed over SAO IPCC reference region, calculated for each grid cell interpolated at 0.25 regular grid for the CNRM-CM6-1-LR (1st row), CNRM-CM6-1-HR (2nd row), and the difference between the two (3rd row)

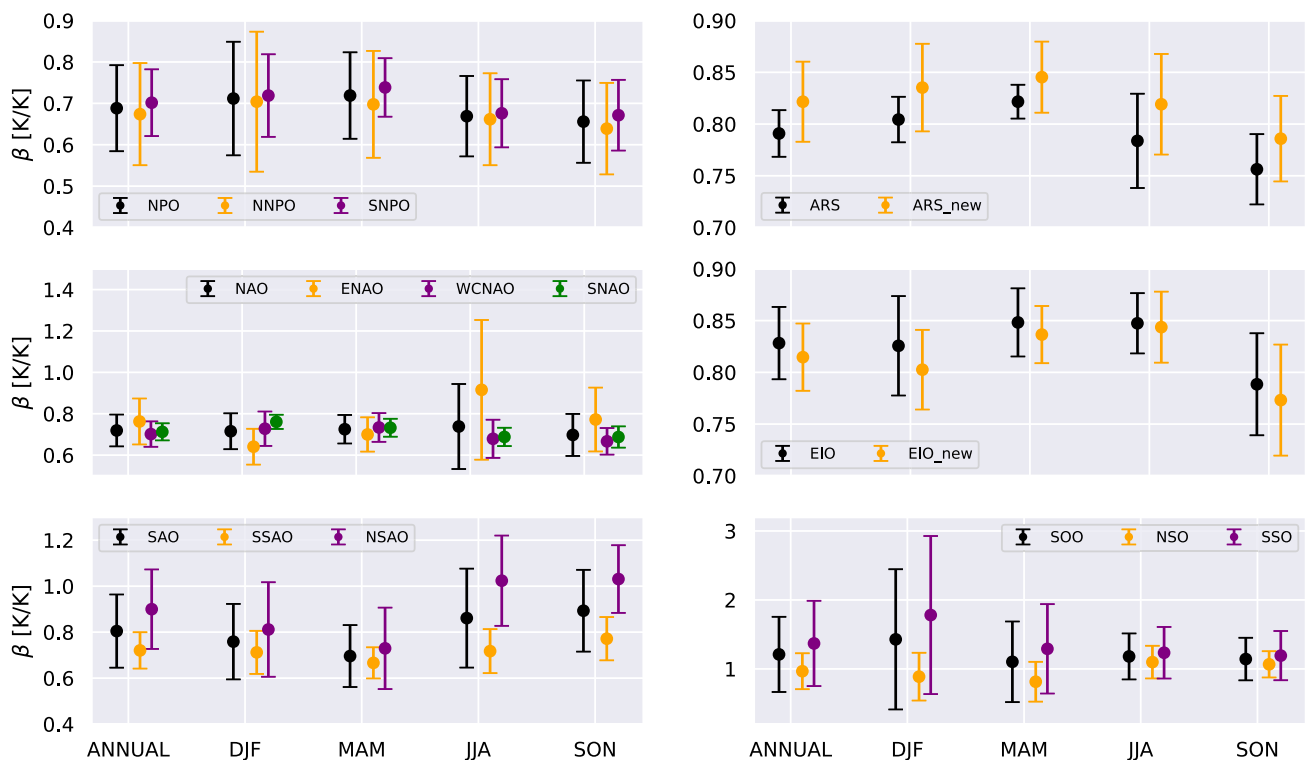


Fig. 15 Spatial mean and spread of β for SSAT. The results are displayed for both the existing six IPCC regions (each region per panel) and their newly suggested counterparts

Table 1 List of 26 CMIP6 GCMs used in the study, with corresponding resolutions of the atmospheric (column 2) and coupled oceanic model (column 3). The coupled ocean models are listed in column 4, and the sea-ice parametrization in column 5

CMIP6 GCMs	Δx atmos. [km]	Δx ocean [km]	Ocean model	Sea-Ice model
ACCESS-CM2	250	250	ACCESS-OM2	CICE5.1.2
ACCESS-ESM1-5	250	250	ACCESS-OM2	CICE4.1
AWI-CM-1-1-MR	100	25	FESOM 1.4	FESOM 1.4
BCC-CSM2-MR	100	100	MOM4	SIS2
CAMS-CSM1-0	100	100	MOM4	SIS 1.0
CanESM5	500	100	NEMO3.4.1	LIM2
CESM2-FV2	250	100	POP2	CICE5.1
CESM2-WACCM-FV2	100	100	POP2	CICE5.1
CMCC-CM2-SR5	100	100	NEMO3.6	CICE4.0
CNRM-CM6-1	250	100	NEMO3.6	Gelato 6.1
CNRM-CM6-1-HR	50	25	NEMO3.6	Gelato 6.1
CNRM-ESM2-1	250	100	NEMO3.6	Gelato 6.1
EC-Earth3	100	100	NEMO3.6	LIM3
EC-Earth3-Veg	100	100	NEMO3.6	LIM3
GFDL-ESM4	100	50	GFDL-OM4p5	GFDL-SIM4p5
INM-CM4-8	100	100	INM-OM5	INM-ICE1
INM-CM5-0	100	100	INM-OM5	INM-ICE1
IPSL-CM6A-LR	250	100	NEMO-OPA	NEMO-LIM3
MIROC-ES2L	500	100	COCO4.9	COCO4.9
MIROC6	250	100	COCO4.9	COCO4.9
MPI-ESM1-2-HR	100	50	MPIOM1.63	(Semtner zero-layer) dynamic (Hibler 79) sea ice model)
MPI-ESM1-2-LR	250	250	MPIOM1.63	(Semtner zero-layer) dynamic (Hibler 79) sea ice model)
MRI-ESM2-0	100	100	MRI.COM4.4	MRI.COM4.4
NorESM2-LM	250	100	MICOM	CICE
NorESM2-MM	100	100	MICOM	CICE
UKESM1-0-LL	250	100	NEMO-HadGEM3-GO6.0	CICE-HadGEM3-GSI8

Acknowledgements This work is part of the project ATLAS (PID2019-111481RB-I00) funded by MCIN/AEI/10.13039/501100011033. JF and JM acknowledge support from the project CORDyS (PID2020-116595RB-I00) funded by MCIN/AEI/10.13039/501100011033. RGJ acknowledges support from the Met Office Hadley Centre Climate Programme funded by the UK government's Department for Science, Innovation and Technology. We also acknowledge the Earth System Grid Federation (ESGF) infrastructure, an international effort led by the U.S. Department of Energy's Program for Climate Model Diagnosis and Intercomparison, the European Network for Earth System Modelling and other partners in the Global Organisation for Earth System Science Portals (GO-ESSP). We acknowledge the World Climate Research Program's Working Group on Coupled Modelling, which is responsible for CMIP, and we thank the climate modeling groups for producing and making available their model output. Special thanks go to Joaquín Bedia Jiménez for his contribution in developing the GWL analysis conception and his comments that helped to improve this manuscript.

Author Contributions All authors contributed to developing the study conception and design. Material preparation and data collection were performed by Josipa Milovac and Maialen Iturbide, code development by Josipa Milovac, Jesús Fernández and Javier Diez-Sierra, and analysis by Josipa Milovac. The first draft of the manuscript was written by Josipa Milovac and all authors commented on previous versions of the manuscript. All authors read and approved the final manuscript.

Funding Open Access funding provided thanks to the CRUE-CSIC agreement with Springer Nature. This work was supported by the projects ATLAS (PID2019-111481RB-I00) funded by MCIN/AEI/10.13039/501100011033, and CORDyS (PID2020-116595RB-I00) funded by MCIN/AEI/10.13039/501100011033. RGJ was supported by the Met Office Hadley Centre Climate Programme funded by the UK governments Department for Science, Innovation and Technology.

Data Availability The dataset generated and analysed in the study and the polygons of the suggested refined Physical-climate-assessment-reference-regions-v4.1 are available in Zenodo: <https://doi.org/10.5281/zenodo.10666947> and the GitHub repository: https://github.com/SantanderMetGroup/2023_Milovac_SSTvsGWL.

Code Availability The code used for the analysis is available in the GitHub repository: https://github.com/SantanderMetGroup/2023_Milovac_SSTvsGWL.

Declarations

Competing interests The authors have no relevant financial or non-financial interests to disclose.

Open Access This article is licensed under a Creative Commons Attribution 4.0 International License, which permits use, sharing, adap-

tation, distribution and reproduction in any medium or format, as long as you give appropriate credit to the original author(s) and the source, provide a link to the Creative Commons licence, and indicate if changes were made. The images or other third party material in this article are included in the article's Creative Commons licence, unless indicated otherwise in a credit line to the material. If material is not included in the article's Creative Commons licence and your intended use is not permitted by statutory regulation or exceeds the permitted use, you will need to obtain permission directly from the copyright holder. To view a copy of this licence, visit <http://creativecommons.org/licenses/by/4.0/>.

References

- Adusumilli S, Fricker HA, Medley B, Padman L, Siegfried MR (2020) Interannual variations in meltwater input to the Southern Ocean from Antarctic ice shelves. *Nat Geosci* 13:616–620. <https://doi.org/10.1038/s41561-020-0616-z>
- Alves JMR, Peliz A, Caldeira RMA, Miranda PMA (2018) Atmosphere-ocean feedbacks in a coastal upwelling system. *Ocean Model* 123:55–65. <https://doi.org/10.1016/j.ocemod.2018.01.004>
- Anderson B, Mackintosh A (2012) Controls on mass balance sensitivity of maritime glaciers in the Southern Alps, New Zealand: The role of debris cover. *J Geophys Res Earth Surf* 117(F1):F01003. <https://doi.org/10.1029/2011JF002064>
- Armitage TWK, Kwok R, Thompson AF, Cunningham G (2018) Dynamic Topography and Sea Level Anomalies of the Southern Ocean: Variability and Teleconnections. *J Geophys Res Oceans* 123(1):613–630. <https://doi.org/10.1002/2017JC013534>
- Armour KC, Marshall J, Scott JR, Donohoe A, Newsom ER (2016) Southern Ocean warming delayed by circumpolar upwelling and equatorward transport. *Nat Geosci* 9(7):549–554. <https://doi.org/10.1038/ngeo2731>
- Auger M, Morrow R, Kestenare E, Sallée JB, Cowley R (2021) Southern Ocean in-situ temperature trends over 25 years emerge from interannual variability. *Nat Commun* 12(1):514. <https://doi.org/10.1038/s41467-020-20781-1>
- Bulgin CE, Merchant CJ, Ferreira D (2020) Tendencies, variability and persistence of sea surface temperature anomalies. *Sci Rep* 10(1):7986. <https://doi.org/10.1038/s41598-020-64785-9>
- Caesar L, McCarthy GD, Thornalley DJR, Cahill N, Rahmstorf S (2021) Current Atlantic Meridional Overturning Circulation weakest in last millennium. *Nat Geosci* 14(3):118–120. <https://doi.org/10.1038/s41561-021-00699-z>
- Cai W, Ng B, Wang G, Santoso A, Wu L, Yang K (2022) Increased ENSO sea surface temperature variability under four IPCC emission scenarios. *Nat Clim Change* 12(3):228–231. <https://doi.org/10.1038/s41558-022-01282-z>
- Carton JA, Ding Y, Arrigo KR (2015) The seasonal cycle of the Arctic Ocean under climate change. *Geophys Res Lett* 42(18):7681–7686. <https://doi.org/10.1002/2015GL064514>
- Chassignet EP, Xu X, Chassignet EP, Xu X (2017) Impact of Horizontal Resolution (1/12 to 1/50) on Gulf Stream Separation, Penetration, and Variability. *J Phys Oceanogr* 47(8):1999–2021. <https://doi.org/10.1175/JPO-D-17-0031.1>
- Chassignet EP, Yeager SG, Fox-Kemper B, Bozec A, Castruccio F, Danabasoglu G, Horvat C, Kim WM, Koldunov N, Li Y, Lin P, Liu H, Sein DV, Sidorenko D, Wang Q, Xu X (2020) Impact of horizontal resolution on global ocean sea ice model simulations based on the experimental protocols of the Ocean Model Intercomparison Project phase 2 (OMIP-2). *Geosci Model Dev* 13(9):4595–4637. <https://doi.org/10.5194/gmd-13-4595-2020>
- Díez-Sierra J, Iturbide M, Fernández J, Gutiérrez JM, Milovac J, Cofiño AS (2023) Consistency of the regional response to global warming levels from CMIP5 and CORDEX projections. *Clim Dyn* 61(7):4047–4060. <https://doi.org/10.1007/s00382-023-06790-y>
- Durack PJ (2015) Ocean Salinity and the Global Water Cycle. *Oceanography* 28(1):20–31. <https://doi.org/10.5670/oceanog.2015.03>
- Froelicher TL, Fischer EM, Gruber N (2018) Marine heatwaves under global warming. *Nature* 560(7718):360–364. <https://doi.org/10.1038/s41586-018-0383-9>
- García-Soto C, Cheng L, Caesar L, Schmidtko S, Jewett EB, Cheripka A, Rigor I, Caballero A, Chiba S, Báez JC, Zielinski T, Abraham JP (2021) An Overview of Ocean Climate Change Indicators: Sea Surface Temperature, Ocean Heat Content, Ocean pH, Dissolved Oxygen Concentration, Arctic Sea Ice Extent, Thickness and Volume, Sea Level and Strength of the AMOC (Atlantic Meridional Overturning Circulation). *Frontiers in Marine Science* 8
- Giorgi F (2006) Climate change hot-spots. *Geophys Res Lett* 33(8). <https://doi.org/10.1029/2006GL025734>
- Gutiérrez J, Jones R, Narisma G, Alves L, Amjad M, Gorodetskaya I, Grose M, Klutse N, Krakovska S, Li J, Martínez-Castro D, Mearns L, Mernild S, Ngo-Duc T, van den Hurk B, Yoon JH (2021) Atlas. In: Masson-Delmotte V, Zhai P, Pirani A, Connors S, Péan C, Berger S, Caud N, Chen Y, Goldfarb L, Gomis M, Huang M, Leitzell K, Lonnoy E, Matthews J, Maycock T, Waterfield T, Yeleki O, Yu R, Zhou B (eds) *Climate Change 2021: The Physical Science Basis. Contribution of Working Group I to the Sixth Assessment Report of the Intergovernmental Panel on Climate Change*, Cambridge University Press, Cambridge, United Kingdom and New York, NY, USA, pp 1927–2058. <https://doi.org/10.1017/9781009157896.021>, type: Book Section
- Haumann FA, Gruber N, Mnnich M (2020) Sea-Ice Induced Southern Ocean Subsurface Warming and Surface Cooling in a Warming Climate. *AGU Advances* 1(2):e2019AV000132. <https://doi.org/10.1029/2019AV000132>
- Iturbide M, Gutiérrez JM, Alves LM, Bedia J, Cerezo-Mota R, Cimadevilla E, Cofiño AS, Di Luca A, Faria SH, Gorodetskaya IV, Hauser M, Herrera S, Hennessy K, Hewitt HT, Jones RG, Krakovska S, Manzanar R, Martínez-Castro D, Narisma GT, Nurhati IS, Pinto I, Seneviratne SI, van den Hurk B, Vera CS (2020) An update of IPCC climate reference regions for subcontinental analysis of climate model data: definition and aggregated datasets. *Earth Syst Sci Data* 12(4):2959–2970. <https://doi.org/10.5194/essd-12-2959-2020>
- Iturbide M, Fernández J, Gutiérrez JM, Bedia J, Cimadevilla E, Díez-Sierra J, Manzanar R, Casanueva A, Baño Medina J, Milovac J, Herrera S, Cofiño AS, San Martín D, García-Díez M, Hauser M, Huard D, Yeleki (2021) Repository supporting the implementation of FAIR principles in the IPCC WGI Atlas. <https://doi.org/10.5281/zenodo.5171760>, 00000
- Jones PW (1999) First- and Second-Order Conservative Remapping Schemes for Grids in Spherical Coordinates. *Mon Weather Rev* 127(9):2204–2210. [https://doi.org/10.1175/1520-0493\(1999\)127<2204:FASOCR>2.0.CO;2](https://doi.org/10.1175/1520-0493(1999)127<2204:FASOCR>2.0.CO;2)
- Kashiwase H, Ohshima KI, Nihashi S, Eicken H (2017) Evidence for ice-ocean albedo feedback in the Arctic Ocean shifting to a seasonal ice zone. *Sci Rep* 7(1):8170. <https://doi.org/10.1038/s41598-017-08467-z>
- Keil P, Mauritsen T, Jungclaus J, Hedemann C, Olonscheck D, Ghosh R (2020) Multiple drivers of the North Atlantic warming hole. *Nat Clim Change* 10(7):667–671. <https://doi.org/10.1038/s41558-020-0819-8>
- Kessler A, Goris N, Lauvset SK (2022) Observation-based Sea surface temperature trends in Atlantic large marine ecosystems. *Prog Oceanogr* 208:102902. <https://doi.org/10.1016/j.pocean.2022.102902>
- Koenigk T, Fuentes-Franco R, Meccia VL, Gutjahr O, Jackson LC, New AL, Ortega P, Roberts CD, Roberts MJ, Arsouze T, Iovino D, Moine MP, Sein DV (2021) Deep mixed ocean volume in

- the Labrador Sea in HighResMIP models. *Clim Dyn* 57(7):1895–1918. <https://doi.org/10.1007/s00382-021-05785-x>
- Levine XJ, Cvijanovic I, Ortega P, Donat MG, Tourigny E (2021) Atmospheric feedback explains disparate climate response to regional Arctic sea-ice loss. *npj Clim Atmos Sci* 4(1):1–8. <https://doi.org/10.1038/s41612-021-00183-w>
- Long M, Zhang L, Hu S, Qian S (2021) Multi-Aspect Assessment of CMIP6 Models for Arctic Sea Ice Simulation. *J Clim* 34(4):1515–1529. <https://doi.org/10.1175/JCLI-D-20-0522.1>
- Masson-Delmotte V, Schulz M, Abe-Ouchi A, Beer J, Ganopolski A, Rouco JFG, Jansen E, Lambeck K, Luterbacher J, Naish T, Osborn T, Otto-Bliessner B, Quinn T, Ramesh R, Rojas M, Shao X, Timmermann A (2013) Information from Paleoclimate Archives. In: Stocker TF, Qin D, Plattner GK, Tignor M, Allen SK, Boschung J, Nauels A, Xia Y, Bex V, Midgley PM (eds) *Climate Change 2013: The Physical Science Basis*. Contribution of Working Group I to the Fifth Assessment Report of the Intergovernmental Panel on Climate Change, Cambridge University Press, Cambridge, United Kingdom and New York, USA, pp 383–464. <https://doi.org/10.1017/CBO9781107415324.013>, section: 5
- Masson-Delmotte V, Zhai P, Prtner HO, Roberts D, Skea J, Shukla PR, Pirani A, Moufouma-Okia W, Péan C, Pidcock R, Connors S, Matthews JBR, Chen Y, Zhou X, Gomis MI, Lonnoy E, Maycock T, Tignor M, Waterfield T, Pirani A, Moufouma-Okia W, Péan C, Pidcock R, Connors S, Matthews JBR, Chen Y, Zhou X, Gomis MI, Lonnoy E, Maycock T, Tignor M, Waterfield T (eds) (2018) *Global Warming of 1.5°C: An IPCC Special Report on the impacts of global warming of 1.5°C above pre-industrial levels and related global greenhouse gas emission pathways, in the context of strengthening the global response to the threat of climate change, sustainable development, and efforts to eradicate poverty*. Cambridge University Press
- Masson-Delmotte V, Zhai P, Pirani A, Connors SL, Péan C, Berger S, Caud N, Chen Y, Goldfarb L, Gomis MI, Huang M, Leitzell K, Lonnoy E, Matthews JBR, Maycock TK, Waterfield T, Yeleki, Yu R, Zhou B (eds) (2021) *Climate Change 2021: The Physical Science Basis*. Contribution of Working Group I to the Sixth Assessment Report of the Intergovernmental Panel on Climate Change. Cambridge University Press
- Medhaug I, Stolpe MB, Fischer EM, Knutti R (2017) Reconciling controversies about the global warming hiatus. *Nature* 545(7652):41–47. <https://doi.org/10.1038/nature22315>, <https://www.nature.com/articles/nature22315>
- Middlemas E, Clement A, Medeiros B (2019) Contributions of atmospheric and oceanic feedbacks to subtropical northeastern sea surface temperature variability. *Clim Dyn* 53(11):6877–6890. <https://doi.org/10.1007/s00382-019-04964-1>
- Palmer M, Slangen A, Domingues C, Savita A, Dias F, Koll R (2021) Chapter 9: Ocean, cryosphere and sea level change - IPCC AR6 Fox-Kemper B, Hewitt HT, Xiao C, Aalgeirsdóttir G, Drijfhout SS, Edwards TL, Golledge NR, Hemer M, Kopp RE, Krinner G, Mix A, Notz D, Nowicki S, Nurhati IS, Ruiz L, Sallée J-B, Slangen ABA, Yu Y 2021: Cambridge University Press
- Rackow T, Danilov S, Goessling HF, Hellmer HH, Sein DV, Semmler T, Sidorenko D, Jung T (2022) Delayed Antarctic sea-ice decline in high resolution climate change simulations. *Nat Commun* 13(1):637. <https://doi.org/10.1038/s41467-022-28259-y>
- Rantanen M, Karpechko AY, Lipponen A, Nordling K, Hyvrinen O, Ruosteenoja K, Vihma T, Laaksonen A (2022) The Arctic has warmed nearly four times faster than the globe since 1979. *Commun Earth Environment* 3(1):1–10. <https://doi.org/10.1038/s43247-022-00498-3>
- Roberts MJ, Jackson LC, Roberts CD, Meccia V, Docquier D, Koenigk T, Ortega P, Moreno-Chamarro E, Bellucci A, Coward A, Drijfhout S, Exarchou E, Gutjahr O, Hewitt H, Iovino D, Lohmann K, Putrasahan D, Schiemann R, Seddon J, Terray L, Xu X, Zhang Q, Chang P, Yeager SG, Castruccio FS, Zhang S, Wu L (2020) Sensitivity of the Atlantic Meridional Overturning Circulation to Model Resolution in CMIP6 HighResMIP Simulations and Implications for Future Changes. *J Adv Model Earth Syst* 12(8):e2019MS002014. <https://doi.org/10.1029/2019MS002014>
- Ruela R, Sousa MC, deCastro M, Dias JM (2020) Global and regional evolution of sea surface temperature under climate change. *Glob Planet Change* 190:103190. <https://doi.org/10.1016/j.gloplacha.2020.103190>
- Seneviratne SI, Hauser M (2020) Regional Climate Sensitivity of Climate Extremes in CMIP6 Versus CMIP5 Multimodel Ensembles. *Earth's Future* 8(9):e2019EF001474. <https://doi.org/10.1016/10.1029/2019EF001474>
- Varela R, Lima FP, Seabra R, Meneghesso C, Gómez-Gesteira M (2018) Coastal warming and wind-driven upwelling: A global analysis. *Sci Total Environ* 639:1501–1511. <https://doi.org/10.1016/j.scitotenv.2018.05.273>
- Varela R, DeCastro M, Rodriguez-Diaz L, Dias JM, Gómez-Gesteira M (2022) Examining the Ability of CMIP6 Models to Reproduce the Upwelling SST Imprint in the Eastern Boundary Upwelling Systems. *J Mar Sci Eng* 10(12):1970. <https://doi.org/10.3390/jmse10121970>
- Virtanen P, Gommers R, Oliphant TE, Haberland M, Reddy T, Cournapeau D, Burovski E, Peterson P, Weckesser W, Bright J, van der Walt SJ, Brett M, Wilson J, Millman KJ, Mayorov N, Nelson ARJ, Jones E, Kern R, Larson E, Carey CJ, Polat I, Feng Y, Moore EW, VanderPlas J, Laxalde D, Perktold J, Cimrman R, Henriksen I, Quintero EA, Harris CR, Archibald AM, Ribeiro AH, Pedregosa F, van Mulbregt P (2020) SciPy 10 Contributors, SciPy 1.0: Fundamental Algorithms for Scientific Computing in Python. *Nat Methods* 17:261–272. <https://doi.org/10.1038/s41592-019-0686-2>
- Xu X, Liu J, Huang G (2022) Understanding Sea Surface Temperature Cooling in the Central-East Pacific Sector of the Southern Ocean During 1982–2020. *Geophys Res Lett* 49(10):e2021GL097579. <https://doi.org/10.1029/2021GL097579>